

## Elliptical-inertial instability of rotating Karman vortex streets

A. Stegner<sup>a)</sup>

*Laboratoire de Météorologie Dynamique, Centre National de la Recherche Scientifique (CNRS), Ecole Normale Supérieure (ENS), 24 Rue Lhomond, 75005 Paris, France*

T. Pichon and M. Beunier

*Unité d'Enseignement et de Recherche en Mécanique (UME), Ecole Nationale Supérieure de Techniques Avancées (ENSTA) Centre de l'Yvette, Chemin de la Hunière, 91120 Palaiseau Cedex, France*

(Received 17 August 2004; accepted 22 February 2005; published online 8 June 2005)

Clouds often reveal a small-scale vortex shedding in the wake of mountainous islands. Unlike the classical bidimensional Karman street, these observed vortex streets are affected by the earth's rotation and vertical stratification of the atmosphere. These effects induce a selective destabilization of anticyclonic vorticity regions. It is well known that inertial instability, also called centrifugal instability, induces a three-dimensional destabilization of anticyclonic vortices when the absolute vorticity is larger than the local Coriolis parameter. However, we have shown by means of laboratory experiments, that it is a different type of instability which is mainly responsible for the secondary destabilization of rotating Karman streets. A series of experiments were performed to study the wake of a cylinder in a rotating deep water layer, at a medium Reynolds number and an order one Rossby number. We have shown that the unstable mode is a core-centered perturbation and its vertical wavelength strongly depends on the Rossby number. These dynamical characteristics are the signature of an elliptical instability in rotating flows. We have also checked that an asymptotic instability criterion, valid around an elliptical stagnation point, was satisfied in the early stage of shedding when the anticyclonic boundary layer detaches and rolls up in elliptical structures. Similar asymmetric Karman streets were also found in the shallow-water configuration when the vertical to horizontal aspect ratio is close to unity. © 2005 American Institute of Physics. [DOI: 10.1063/1.1937348]

### I. INTRODUCTION

One of the first rewards of meteorological satellites was the regular surveillance of cloud patterns over hitherto poorly observed oceanic areas. Many fascinating new patterns emerged, one of the most striking being the vortex streets downwind of small isolated islands.<sup>1</sup> In general, these vortex shedding are qualitatively similar to a classical Karman street in which both the anticyclonic and the cyclonic vortices are equally developed. The characteristic horizontal scale of these coherent structures remains small (10–50 km) compared to the atmospheric Rossby radius (~1000 km). Hence, the pressure gradient is expected to be mainly balanced by the centrifugal force, while, the Coriolis force and the geostrophic balance are generally neglected. Several studies of atmospheric Karman streets take into account the vertical stratification<sup>2–6</sup> and neglect the influence of the rotation. In comparison with the classical Karman street, the stratification introduces inviscid mechanisms of vorticity production. For atmospheric lee vortices, the tilting of baroclinically generated vorticity or the vorticity produced through dissipation in hydraulic jumps could overcome the vorticity generated in frictional boundary layer.<sup>3,6,7</sup> Nevertheless, all these mechanisms lead to a wake where vortices of both signs are equivalent in shape. But, in some cases the satellite photographs reveal an asymmetric shedding in

which the anticyclonic structures are distorted and less circular than their cyclonic counterpart (see Fig. 1). Such asymmetry cannot be explained if the rotation is not taken into account.

It is well known that the rotation alters the stability of incompressible two-dimensional flow with respect to three-dimensional perturbations. The Coriolis force induces a selective destabilization of anticyclonic vorticity regions. Johnson<sup>8</sup> and Yanase, Flores, Metais, and Riley<sup>9</sup> show by means of linear stability analysis that three-dimensional instability occurs locally for parallel shear flow when the absolute vorticity is negative. For circular vortices, the generalized Rayleigh criterion proposed by Kloosterziel and van Heijst<sup>10</sup> or Mutabazi, Normand, and Wesfreid<sup>11</sup> asserts that all anticyclonic vortex columns are unstable to vertical perturbation if the absolute vorticity becomes negative. In this case, the perturbation is expected to be located in an annular region, surrounding the vortex core, where the Rayleigh discriminant is negative.<sup>12</sup> More recently, several theoretical analyses<sup>13,14</sup> have been devoted to the effects of rotation on centrifugal (or inertial), elliptic, and hyperbolic types of instability in two-dimensional flows. For all these cases, the rotation induces or enhances the instability of anticyclonic vorticity regions. This selective destabilization of intense anticyclones was also checked by means of laboratory experiments<sup>10,14–20</sup> or direct numerical simulations.<sup>21–23</sup>

Nevertheless, the exact nature of this selective destabilization and the vertical wavelength selection of unstable per-

<sup>a)</sup> Author to whom correspondence should be addressed; electronic mail: stegner@lmd.ens.fr

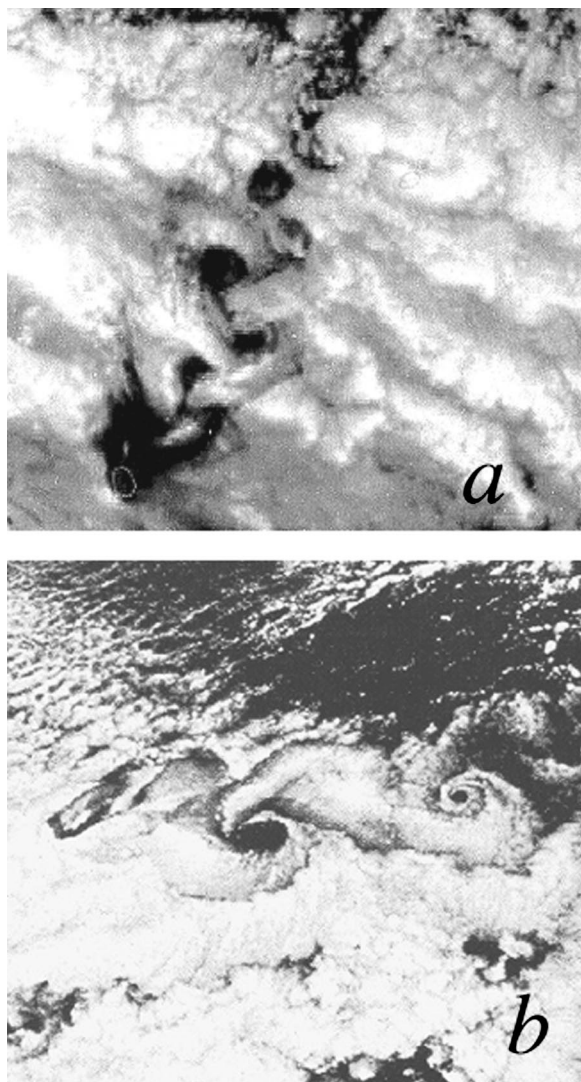


FIG. 1. Cloud visualization of asymmetry between cyclones and anticyclones emitted in an oceanic islands wake. For Alejandro Selkirk island (33°45'S;80°46'W) in the south hemisphere (a) cyclones are on the left side of the image, whereas for Guadeloupe island (16°22'N;61°37'W) in the northern hemisphere (b) cyclones are at the bottom.

turbations is still not well understood for the case of Karman streets in a rotating barotropic fluid (i.e., without stratification). In this case, three dynamical stages occur (Fig. 2). The vorticity is initially produced in the boundary layer around the obstacle. Just behind it, the detachment of this boundary layer leads to free-shear layers. In a second stage, these parallel shear layers roll up alternatively on both sides of the obstacle into elliptical structures. Then, these transient elliptical structures evolve quickly to axisymmetric vortices leading to a final stage corresponding to a quasisteady Karman street. Hence, at each stage, specific three-dimensional instabilities (inertial, elliptical, or centrifugal) could destabilize the anticyclonic vorticity regions. We performed several laboratory experiments in order to investigate which instability mechanism controls the asymmetry of rotating Karman streets.

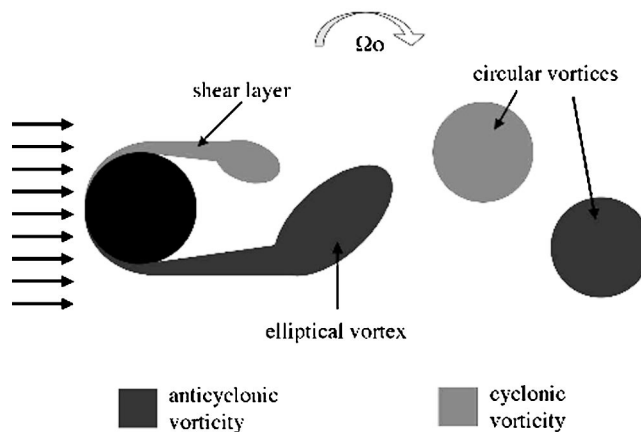


FIG. 2. Positive and negative vorticity regions in a cylinder wake.

## II. POSSIBLE INSTABILITIES AND RELATED STABILITY CRITERION

In a first stage, the boundary layer detachment leads to a free-shear flow just behind the cylinder. The impact of rotation on free-shear-flows instability was studied by Johnson<sup>8</sup> for the inviscid case. Considering a rigid body rotation along the  $z$  axis and a shear flow with horizontal velocity  $U$  in the  $x$  direction which varies in the  $y$  direction, three-dimensional perturbations are unstable if somewhere in the flow

$$\Phi = 2\Omega_0(2\Omega_0 + \omega) < 0, \tag{1}$$

where  $\omega = -dU/dy$  is the vorticity in the rotating frame. Hence, three-dimensional instabilities could occur only in anticyclonic vorticity regions where  $\omega/2\Omega_0 < -1$ . The viscous linear stability analysis of both shear flow and planar wake subjected to rotation was studied in detail by Yanase, Flores, Metais, and Riley.<sup>9</sup> Unstable perturbations in the form of streamwise rolls were found in anticyclonic regions for both cases. Such perturbations had stronger growth rates than the two-dimensional (2D) barotropic instability of the nonrotating shear layer for roughly the range  $-8 < \omega/2\Omega_0 < -1.5$ . The maximum growth rates were obtained for  $\omega/2\Omega_0 \approx -2$ . The vertical wavelength  $\lambda$  of the most unstable perturbation decreased with the Reynolds number  $Re = UL/\nu$  and increased slightly with the Rossby number  $Ro = U/(2\Omega_0 L)$ . Nevertheless, the dependence of  $\lambda$  on  $Ro$  is weak and a factor 10 in the Rossby number will just increase the wavelength by a factor of 1.5. Besides, the vertical wavelength of the streamwise perturbation is much smaller than the horizontal wavelength of the bidimensional perturbation. Hence, the inertial instability, which is active in anticyclonic vorticity regions, generates smaller-scale perturbations than the two-dimensional barotropic shear instability.

In a second stage, the free-shear layer rolls up into elliptical vortices. Pierrehumbert<sup>24</sup> and Bayly<sup>25</sup> showed that the nonaxisymmetry could be a source of instability. A resonant interaction between the inertial waves of the vortex and the underlying strain field could generate three-dimensional perturbations in regions of two-dimensional, elliptical streamlines. The unstable perturbation grows invariably in the vortex core, leading to sinuous undulations of the initial vortex along its vertical axis. In the presence of rotation the elliptical

cal instability is weakened for cyclonic vortices and enhanced for strong anticyclonic vortices. An inviscid instability criterion has been derived by Cambon, Benoît, Shao, and Jacquin<sup>26</sup> for rotating two-dimensional flows submitted to a strain field. For an asymmetric vortex the elliptical instability will occur if

$$-2D < 4\Omega_0 + \omega < 2D, \quad (2)$$

where  $D$  is the background strain rate. Hence, an anticyclonic elliptical vortex will always be unstable when  $\omega/2\Omega_0 = -2$ . Recent stability analyses<sup>12,13,26</sup> using a geometrical optics method (WKB approximation) for localized short-wave perturbations showed that the growth rate is maximum for the elliptical stagnation point when  $\omega/2\Omega_0 = -2$ . According to LeDizes,<sup>27</sup> for an asymptotically small ellipticity, the maximum growth rate will be reached when

$$\cos \theta = \frac{\omega}{2(2\Omega_0 + \omega)}, \quad (3)$$

where  $\theta$  is the angle between the wave vector of the short-wave perturbation and the rotation axis. Hence, the tilting angle of the most unstable perturbation, and therefore the vertical wavelength selection, will be significantly influenced by the Rossby number (i.e., the ratio  $\omega/2\Omega_0$ ).

In a third stage the transient elliptical vortices formed just behind the cylinder evolve quickly to quasicircular vortices. In order to account for the effect of Coriolis force on the stability of circular vortices, Kloosterziel and van Heijst<sup>10</sup> and Mutabazi, Normand, and Wesfreid<sup>11</sup> extended the classical Rayleigh criterion for centrifugal instability to rotating flows. This generalized Rayleigh criterion states that instability occurs when

$$\Phi = 2(\Omega_0 + V/r)(2\Omega_0 + \omega) < 0. \quad (4)$$

In other words, it states simply that the flow is unstable if the square of the absolute circulation decreases somewhere. According to Eq. (4), all anticyclonic vortices become unstable when  $\omega/2\Omega_0 < -1$ . The centrifugally unstable perturbations are located in regions where the generalized criterion is negative. Even for asymmetric structures, these three-dimensional perturbations are located in annular regions at the vortex periphery<sup>13,28</sup> whereas the unstable elliptical modes are core centered. As far as we know, the influence of the Rossby number on the vertical wavelength selection has not been studied analytically or numerically for circular vortices. However, laboratory experiment on unbounded rotating Couette flow<sup>17</sup> showed that the centrifugal instability is not especially selective in terms of the vertical wavelength. The latter scales as the inverse square of the Reynolds number and weakly depends on the Rossby number.

### III. THE EXPERIMENT

We performed a series of experiments on a 1.5-m-diameter rotating turntable at the Department of Mechanics UME, ENSTA Palaiseau. The upper plate of this turntable rotates on a thin air layer in order to reduce friction and avoid all mechanical vibrations. The turntable had a clockwise rotation and the angular velocity  $\Omega_0$  could reach a

value up to 12 rpm. Due to the clockwise rotation of the turntable, the sense of rotation of cyclonic and anticyclonic structures is then directly comparable to atmospheric flows in the southern hemisphere. We used a rectangular tank  $L = 48$  cm wide, 130 cm long and the working depth  $H$  was fixed at 14 cm. The cylinder diameter  $D$  was varied from 1 to 4 cm and the drift velocity  $U$  from 0.3 to 2 cm/s.

To measure the horizontal velocity field, we used a horizontal 670-nm laser sheet focused 2 cm below the free surface to lighten small neutral particles dispersed in the whole fluid volume and analyze the fluid motion with a standard particle image velocimetry software (PIV LAVISION). Using a  $768 \times 576$  pixel charge-coupled device (CCD) camera and successive cross-correlation processing between two images we got a  $68 \times 48$  horizontal vector field. To visualize the vertical wavelength and the small-scale features of the perturbation, we proceeded as follows: when the solid-body rotation was achieved, we slowly introduced the cylinder, initially painted with a fluorescent dye, into the fluid layer. Then the dye began to diffuse in the water and we started the horizontal motion of the cylinder. In this way we obtained a homogeneous release of fluorescent tracer in the cylinder boundary layer. A top-view and a side-view camera were used simultaneously for several experiments in order to visualize the three-dimensional structure of the flow.

The forcing conditions are fixed by the working depth  $H$ , the cylinder diameter  $D$ , the cylinder velocity  $U$ , the angular rotation  $\Omega_0$ , the gravity  $g$ , the smallest tank size  $L$ , and the viscosity  $\nu$ . For all the cases, the deformation radius  $R_d = \sqrt{gH/2\Omega_0}$  was one order of magnitude larger than the cylinder diameter and we can therefore neglect the free-surface deformation, in other words, the effects of gravity. Therefore, according to dimensional analysis, the formation of the rotating vortex street is mainly governed by four dimensionless parameters. We introduced the Rossby number  $Ro = U/\Omega_0 D$ , the Reynolds number  $Re = UD/\nu$ , the cylinder aspect ratio  $\alpha = H/D$ , and the channel blockage factor  $s = D/L$ . On one hand, the channel blockage factor was kept small  $s = 0.02-0.08$  to minimize sidewall effects. On the other hand, the cylinder aspect ratio was kept large  $\alpha = 14-4$  in order to visualize accurately the vertical structure of unstable perturbations. For a large cylinder aspect ratio, the instabilities of the cylinder wake and the selective destabilization of anticyclonic structures are mainly governed by the parameter couple  $(Re, Ro)$ . A first set of experiments were performed at a low Reynolds number,  $Re \sim 150$ , below the threshold of three-dimensional instabilities ( $Re \sim 190-260$ ) for a classical nonrotating cylinder wake.<sup>13</sup> We easily changed the Rossby number from  $Ro = 0.3$  to 3, by adjusting the angular rotation of the platform from 1 to 10 rpm, without changing the Reynolds number. A second set of experiments were performed for higher values of the Reynolds number,  $Re \sim 400-1400$ . Besides, as far as the barotropic rotating experiment is concerned, the effects of the viscous Ekman layer at the bottom of the tank play an important role. The standard Ekman spin-down time is given by  $T_E = H/(2\Omega_0\nu)^{1/2}$  while the corresponding Ekman number is  $E_k = \nu/(2\Omega_0 H^2)$ . This spin-down time  $T_E = 100-400$  s is sufficiently large compared to the characteristic eddy turnover time  $T_{eddy} = 1-6$  s to

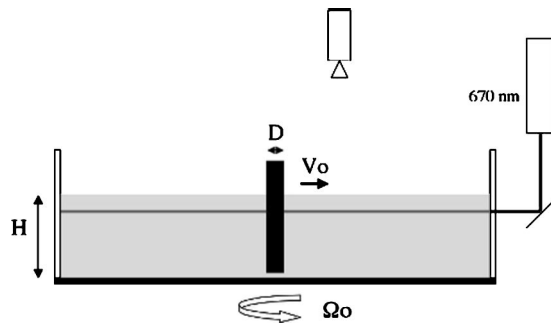


FIG. 3. Scheme of the experimental apparatus.

allow us to neglect the Ekman pumping at the first stage of vortex shedding. Nevertheless, both the horizontal viscous diffusion and the Ekman pumping will dissipate the energy of circular vortices in a fully developed Karman street.

## IV. RESULTS

### A. Dye visualization of the cyclone-anticyclone asymmetry

We performed a series of experiments varying only the Rossby number while the Reynolds number,  $Re \sim 150$ , and the geometrical parameter ( $\alpha \sim 14$  and  $s \sim 0.02$ ) were kept constant. The homogeneous release of a fluorescent tracer in the cylinder boundary layer was used to observe the qualitative nature of the flow field at a large and a small scale. The spatial distribution of this passive tracer within the cyclonic and the anticyclonic structures behind the obstacle is displayed for three Rossby numbers ( $Ro=1.1, 2$ , and  $3.4$ ) in Fig. 4. The cylinder was towed from the right to the left. Hence, due to the clockwise rotation of the turntable, the cyclonic vortex street was above the anticyclonic one, as in Fig. 2. On one hand, we observed in the lee of the cylinder, the shedding of stable and coherent cyclones. After a tran-

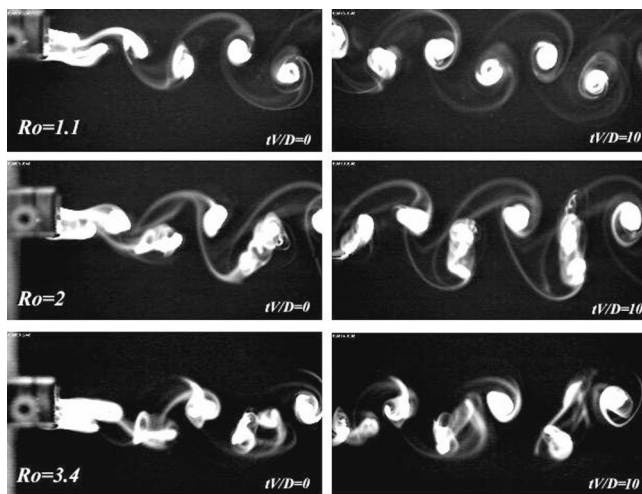


FIG. 4. Top-view visualization of fluorescent dye released in the boundary layer of the cylinder. A 1-cm-diameter cylinder was towed from right to left at a constant speed corresponding to  $Re \sim 150$ . The clockwise rotation of the turntable  $\Omega_0$  was fixed at 12 rpm ( $Ro=1.1$ ), 6 rpm ( $Ro=2$ ), and 4 rpm ( $Ro=3.4$ ). The right-hand-side image was taken 7 s after the left-hand-side image.

sient elliptical shape, due to the roll up of the detached boundary layer behind the cylinder, the cyclonic structures became quickly circular and the dye remained concentrated in the center for a long time. On the other hand, the dye exhibited strong spatial perturbations inside anticyclonic structures. This destabilization of the anticyclonic regions was clearly visible for  $Ro=2$  and  $Ro=3.4$ . Some vortex splitting or separation could occur for a large Rossby number (here,  $Ro=3.4$ ) whereas highly elliptical and stretched patterns were visible when  $Ro=1.5-2.5$ . Such destabilization was not visible for  $Ro < 0.9$  and according to such a type of visualization, we could make only a qualitative estimate of the instability threshold between  $Ro=0.9$  and  $Ro=1.2$  (when  $Re \sim 150$ ). For the case  $Ro=1.1$ , we observed some slight perturbations in the anticyclonic vortex (a small black region in the center), but very quickly a classical Karman street with circular vortices of both signs was formed. These visualizations are similar to the dye observations made by Boyer and Kmetz<sup>16</sup> and Boyer *et al.*<sup>15</sup> in which the cyclones appear much stronger and better defined than the anticyclones in a rotating wake flow. Nevertheless, the critical Rossby number for this cyclone-anticyclone asymmetry was not estimated by these authors. A preliminary study of Bonneton<sup>20</sup> had shown that for  $Re=100$ ,  $\alpha=40$ , and  $s=0.014$ , three-dimensional perturbations distorted the anticyclonic vortex columns when  $Ro$  is equal to or larger than unity.

For an unsteady flow, which is the case here for the vortex street formation behind an obstacle, passive tracer observation should always be taken with care. Indeed, streak-lines (i.e., the dye patterns) which integrate the history of the flow field cannot be compared to the streamlines, an instantaneous representation of the velocity field. For instance, small scale structures of a passive tracer could be observed at a given time even if the flow was perfectly laminar at all scales. Such small-scale dye patterns could be the “ghost” of an old instability or perturbation which is not active anymore. Nevertheless, if we look in detail at a sequence of images (i.e., a movie), the distinction between a ghost and an active small-scale dye pattern could be easily made. In the sequence of images shown in Fig. 5 ( $Re=390$ ,  $Ro=1.65$ ,  $\alpha=4$ , and  $s=0.06$ ) we can see first the growth and the rapid formation of small-scale structures in the anticyclone [Figs. 5(a)–5(c)]. In a second stage [Figs. 5(d)–5(f)] we see just the advection of small-scale structures by a large-scale quasicircular flow. Hence, this second stage probably corresponds to a relaminarization of the anticyclonic flow. Therefore, the selective destabilization of the anticyclones in a rotating von Karman street is a transient phenomenon which occurs in the very initial stage during the vortex shedding. The growth of small-scale perturbations seems to be maximal when the anticyclonic shear layer rolls up into an elliptical structure. After a few inertial periods ( $T_f = T_o/2$ ), stabilization occurs and quasicircular vortices of both signs are present in the rotating von Karman street. This stabilization is probably due to a cyclostrophic adjustment process which restores the bidimensional structure of the flow field within one or two periods of rotation  $T_o$ .

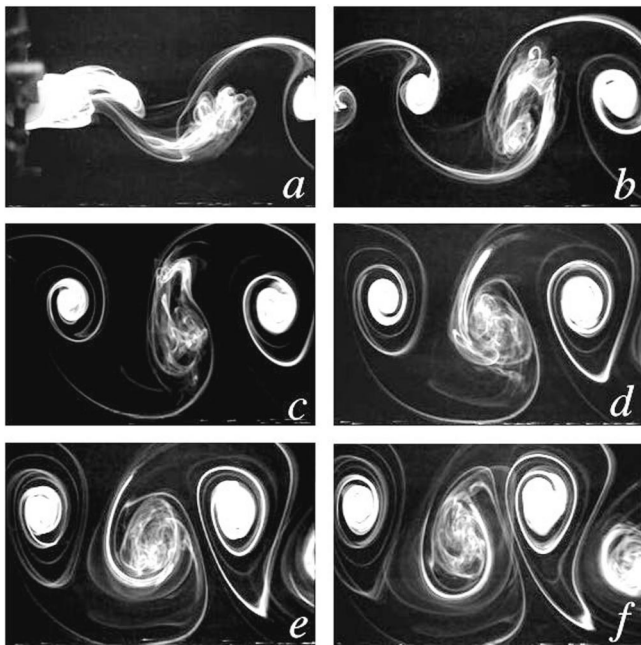


FIG. 5. Dynamical evolution of the vortex street revealed by the fluorescent dye at  $t=0$  (a),  $t=0.8Tf$  (b),  $t=1.6Tf$  (c),  $t=2.2Tf$  (d),  $t=3Tf$  (e), and  $t=3.8Tf$  (f), where  $Tf=\pi/\Omega_0$  is the inertial period. The corresponding parameters for this experiment were  $Ro=2.5$ ,  $Re=150$ , and  $\alpha=10$ .

## B. Vorticity field measurements

In addition to dye visualization, we made a few quantitative measurements of the horizontal velocity field using standard particle image velocimetry. As far as the stability of circular or elliptical vortices depends on their vorticity, according to criteria (1), (2), and (4), we measured this vorticity accurately at different stages of the formation of the rotating Karman street. The first step was to estimate the relation between the vorticity  $\omega_i$  in the core of elliptical structures, formed just behind the cylinder, and the dimensionless Rossby number  $Ro$  constructed with the characteristic forcing scales  $U$  and  $D$  of the drifting cylinder. For the first set of experiments at a low Reynolds number,  $Re \sim 150$ , we found a simple linear relation  $\omega_i/f \sim Ro$  [Fig. 6(a)], where  $f$  is the Coriolis parameter,  $f=2\Omega_0$ . The vorticity  $\omega_i$  was measured approximately one diameter behind the cylinder in the early stage of vortex detachment, to visualize this region, a black cross is shown in Fig. 8(a). For higher Reynolds numbers the relative vorticity of the detached structures increased and we could hardly establish a linear relation between  $\omega_i$  and  $Ro$ . Moreover, as can be seen in Figs. 6(b) and 7, the vorticity of coherent vortices decays with time during the shedding process and the vortex street formation. This decay comes not only from standard viscous dissipation but also from the direct cascade to small-scale perturbations induced by three-dimensional instability. For small Reynolds ( $Re \sim 150$ ) experiments we could hardly detect an asymmetry in the evolution of the maximum vorticity between cyclonic and anticyclonic vortices. However, we start to measure an asymmetric decay for larger Reynolds number ( $Re \sim 400-500$ ) when the classical viscous dissipation is weaker and the selective destabilization of anticy-

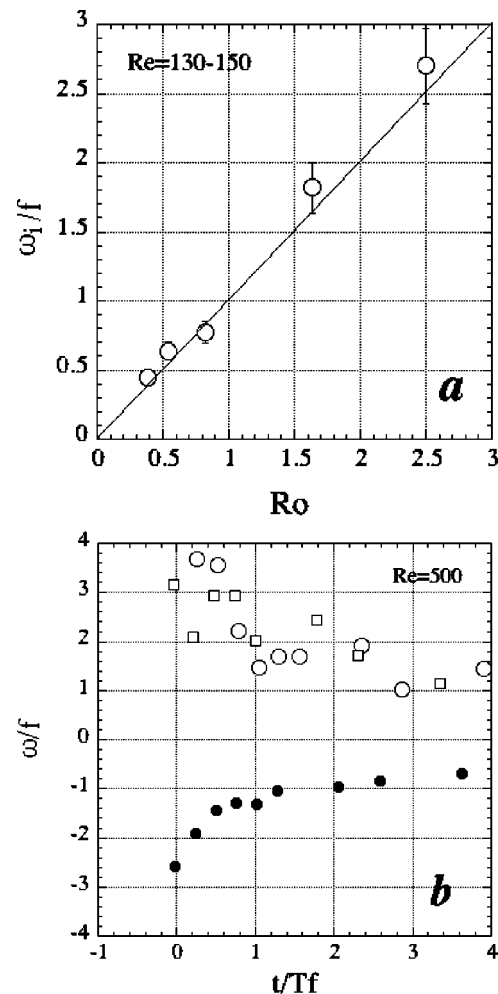


FIG. 6. Relative vorticity, measured from PIV in the core of an elliptical structure just behind the cylinder, as a function of  $Ro$  for small Reynolds number experiments,  $Re \sim 150$  (a). Decay of the relative vorticity in the core of cyclonic (positive values) and anticyclonic (negative values) structures for  $Ro=2.5$  and  $Re=500$  (b). Different symbols are used in (b) for different vortices in the same Karman street.

clones induces an efficient energy transfer to small-scale motion. According to Fig. 6(b), for the unstable case  $Ro=2.5$ ,  $Re=500$ , and  $\alpha=7$ , the relative vorticity of anticyclones reaches quickly ( $t \sim Tf$ ) the marginal stability limit  $\omega/f \sim -1$ , while the cyclones keep a relatively high vorticity value for longer times up to  $t=3Tf \sim 23D/U$ .

According to Fig. 7, for large Reynolds experiment ( $Ro=2.5$ ,  $Re=500$ ), the vorticity field could also reveal the selective destabilization of anticyclonic structures in the cylinder wake. Two parallel shear layers having a high relative vorticity value  $\omega/f$  are visible on the left of Fig. 7(a) just behind the cylinder (not visible here). On the cyclonic side (positive vorticity in red), this shear layer rolls up into elliptical structures that quickly evolve to coherent and axisymmetric vortices. On the other hand, the anticyclonic shear layer (negative vorticity in red) rolls up and then quickly breaks into small-scale vorticity structures [Fig. 7(a)]. After one or two inertial periods these small structures merge together and form elongated elliptical anticyclones having a weaker intensity than the circular cyclones [Fig. 7(c)].

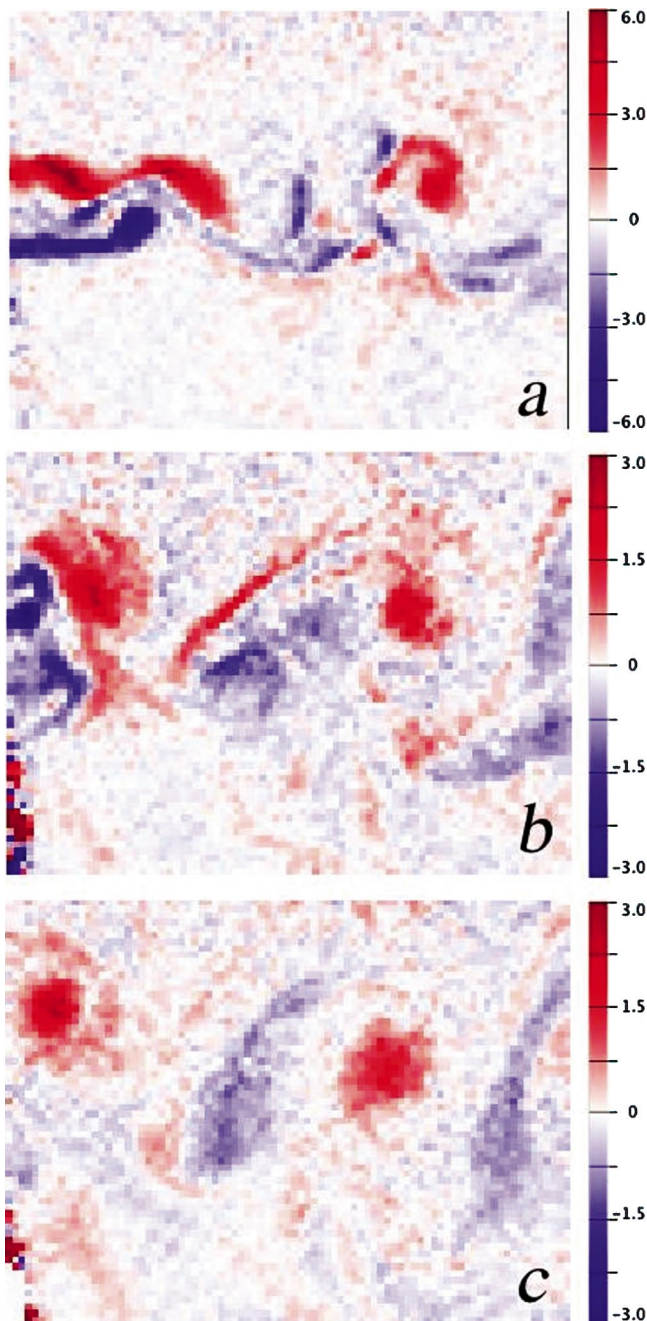


FIG. 7. (Color). Relative vorticity  $\omega/f$  obtained from PIV measurements of the flow field at  $t=0$  (a) just behind the cylinder,  $t=Tf$  (b), and  $t=2Tf$  (c), for  $Ro=2.5$ ,  $Re=500$ , and  $\alpha=7$ . The color table, cyclonic vorticity in red and anticyclonic in blue, is rescaled to extreme values for each image.

Hence, the formation of concentrated cyclones of high intensity and the breakup of anticyclonic structures into elongated elliptical patterns are visible both in the dye visualizations [Fig. 5(c)] and the vorticity field measurements [Fig. 7(c)]. The transverse shift of the cyclonic vortex on the left of Fig. 7 is due to the finite size of the experiment. These vorticity fields were taken close to one sidewall and, at  $t=0.5Tf$ , the cylinder motion was suddenly stopped, thus disturbing the end of the Karman street.

To check the prediction of the elliptical instability criterion (2) proposed by Cambon, Benoit, Shao, Jacquin<sup>26</sup> we calculated from a velocity field ( $Ro=1.6$ ,  $Re \sim 150$ ) taken

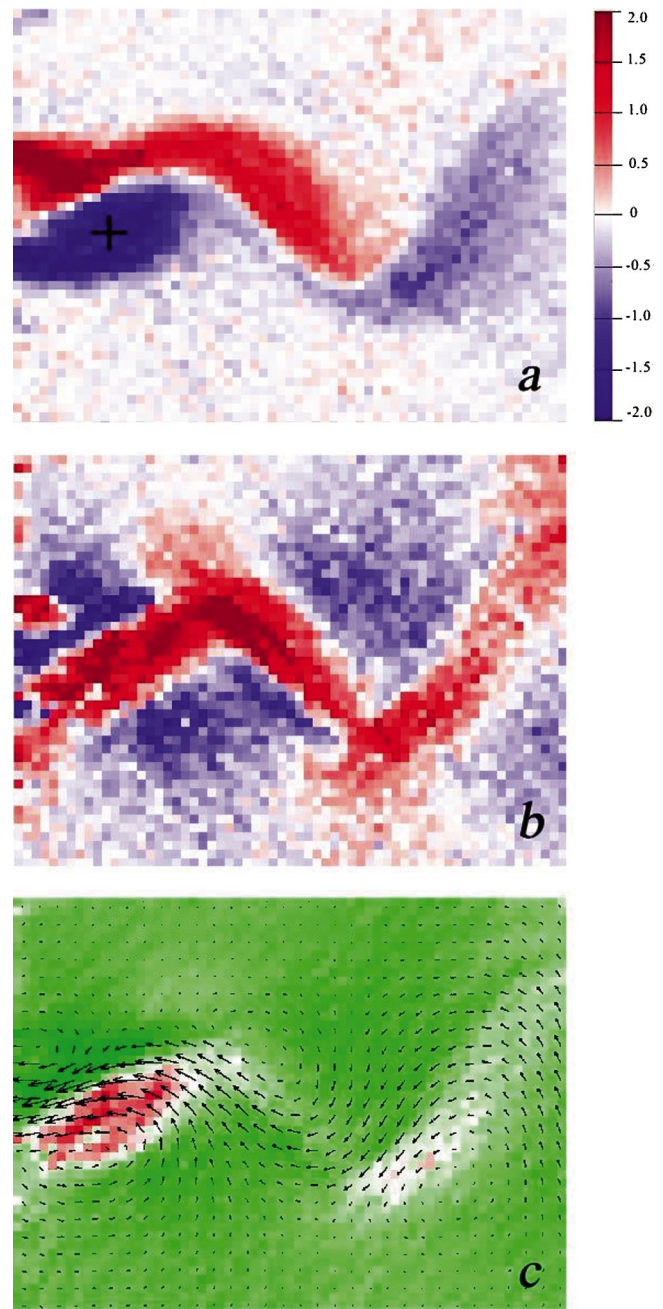


FIG. 8. (Color). Relative vorticity  $\omega/f$  (a) and relative strain  $D/f$  (b) of the flow field just behind the cylinder for  $Ro=1.6$ ,  $Re=150$ , and  $\alpha=14$ . The cylinder (not visible) is just at the left edge of the image. The same color table is used for (a) and (b), with positive (negative) value in red (blue). The black cross in (a) corresponds to the core of the initial elliptical structure where  $\omega_i$  is measured. To localize the region of possible elliptical instability according to the relation (2), the scalar field  $\tilde{\phi}$ , where  $\phi=2D-(4\Omega_0-\omega)$  is plotted in (c). Unstable regions (positive values) are red while stable regions (negative values) are green.

just behind the drifting cylinder, the vorticity  $\omega=\partial_x v-\partial_y u$  [Fig. 8(a)], the strain rate  $D=\frac{1}{2}(\partial_x v+\partial_y u)$  [Fig. 8(b)] and the scalar field  $\phi=2D-(2f-\omega)$  [Fig. 8(c)]. All these fields are rescaled in Fig. 8 with the Coriolis parameter  $f=2\Omega_0$ . Both the vorticity and the strain rate are maximum in the first stage of vortex detachment. Hence, it is during this dynamical stage that  $\phi$  has relatively strong positive values [red zones in Fig. 8(c)] corresponding to unstable regions. The

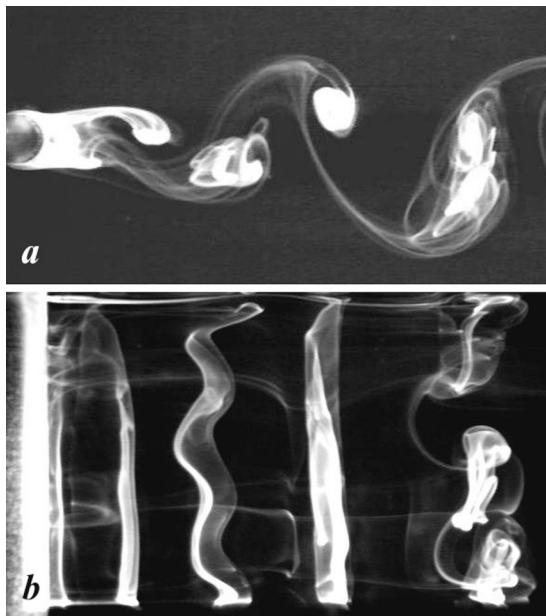


FIG. 9. Simultaneous top-view (a) and side-view (b) dye visualizations of the three-dimensional unstable perturbations growing in anticyclonic columns for  $Ro=2.2$ ,  $Re=148$ , and  $\alpha=10$ .

latter are indeed located in the core of anticyclonic vorticity structures where, according to dye visualizations (Figs. 4 and 5), small-scale perturbations grow rapidly.

### C. Wavelength selection at low Reynolds number

To measure the vertical structure of the unstable perturbations growing in anticyclonic regions we made, for the low Reynolds number experiments ( $Re \sim 150-160$ ), several simultaneous side-view and top-view observations. One of the best examples of such visualization is given in Fig. 9 for the unstable case,  $Ro=2.2$ ,  $Re=148$ ,  $\alpha=7.5$ , and  $s=0.04$ . It is visible that cyclones behave as two-dimensional Taylor columns, while the anticyclones exhibit strong three-dimensional perturbations. In this case, the initial perturbation has a well-defined wavelength and evolves up to a nonlinear stage in which vortex tube splitting occurs. An important fact to notice is that, unlike the centrifugal instability of a circular anticyclonic columnar vortex developing a vortex-edge perturbation,<sup>10,13,14</sup> the unstable mode is here a vortex-core perturbation. Hence, the spatial structure of this unstable mode is in good agreement with the eigenmodes encountered in elliptic instabilities. Similar spatial structures of perturbations generated by the elliptical or the centrifugal instability were observed by Afanasyev<sup>19</sup> in laboratory experiments. He investigated the three-dimensional instability of a vortex pair produced by a rotating flap. The anticyclonic vortex was subject to either centrifugal or elliptical instability if, respectively, the initial streamlines were quasicircular or with a strong ellipticity. This geometrical selection is in agreement with a previous stability analysis performed by Potylitsin and Peltier<sup>28</sup> who have shown that the growth rate of the centrifugal mode could vanish for strongly elliptical vortices. In our case we never observed any vortex-edge per-

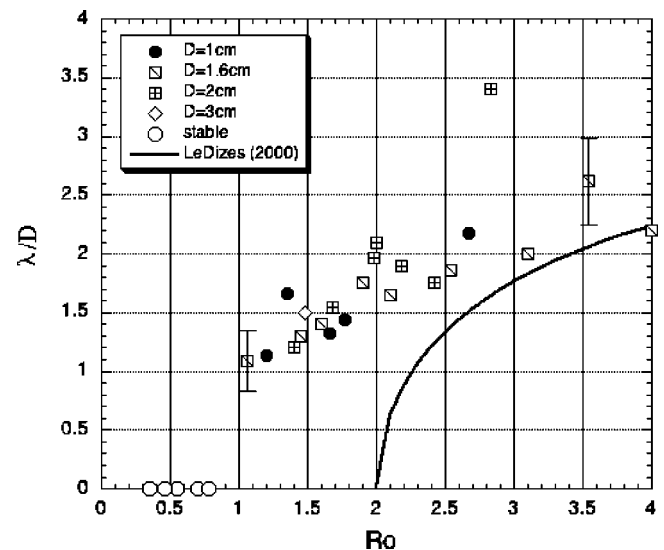


FIG. 10. Vertical wavelength  $\lambda$  of the unstable perturbation function of  $Ro$  for various cylinder diameters,  $D$ , and a constant Reynolds number,  $Re \sim 150-160$ . The error bars give the standard deviation of the measurements for two extreme cases. The solid line corresponds to Eq. (3) using  $k_r \approx 2\pi/R$  and  $k_z \approx 2\pi/\lambda$ .

turbation, probably owing to the strong ellipticity (or background strain field, see Fig. 8) of detached structures during the first stage of shedding.

To complete the characterization of three-dimensional instabilities observed in a rotating Karman street, the vertical wavelength of the perturbation was measured as a function of the Rossby number between  $Ro \sim 1$  and  $Ro \sim 4$ . For larger value of  $Ro$  (i.e., weak rotation) the bottom Ekman layer and the destabilization of the anticyclonic vortex column both affect the vertical alignment of cyclonic vortices and the dye visualization does not allow accurate measurements of the wavelength. According to Fig. 10, above a critical  $Ro \sim 1$ , the vertical wavelength increased with  $Ro$ . The same dependence was also found by Afanasyev<sup>19</sup> for the core-centered instability of elliptical anticyclones. This strong influence of the Rossby number on the wavelength selection contrasts with the vortex-edge perturbation of quasicircular anticyclones which do not depend on  $Ro$ .<sup>18,19</sup> Unfortunately, among all the linear stability analyses of vortices in rotating systems, the influence of  $Ro$  on the vertical wavelength was not really investigated. Nevertheless, for asymptotically small ellipticity, the angle between the wave vector of the most unstable short-wave perturbation and the rotation axis  $\cos \theta = k_z / \sqrt{k_r^2 + k_z^2}$  is a function of the vorticity according to (3). We can try to extend the relation (3) beyond its asymptotic limit and use, as a first guess,  $k_r \approx 2\pi/R$  and  $k_z \approx 2\pi/\lambda$ , where  $\lambda$  is the vertical wavelength. Besides, for this range of Reynolds number, according to Fig. 6(a) the relative vorticity  $\omega/f$  is directly proportional to the Rossby number. We found (Fig. 10) that the heuristic extension of (3) captures the correct dependence of  $\lambda$  with  $Ro$  and surprisingly gives a reasonably good approximation. However, we should keep in mind that during the detachment process, the vortex ellipticity is strong (see Fig. 8, for instance). This geometrical effect could explain why the core-centered mode remains

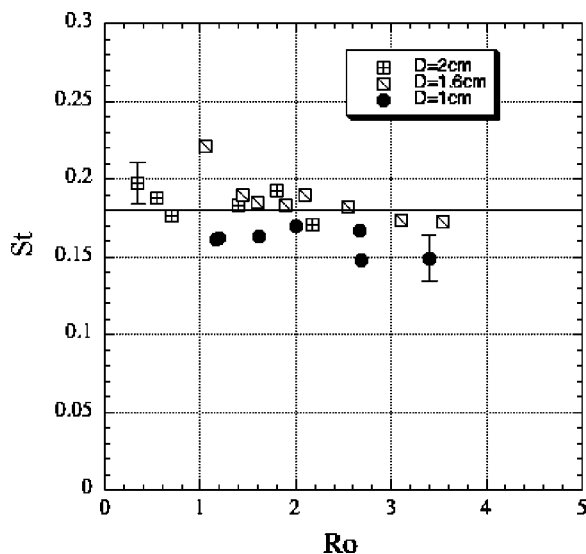


FIG. 11. Strouhal number function of the Rossby number,  $Ro$ , for low Reynolds number experiments,  $Re \sim 150$ .

strongly unstable even in the range of  $1 < Ro < 2$ . Besides, both the vorticity and the ellipticity of detached vortices evolve in time. Therefore, an exact linear stability analysis of the problem is hardly tractable.

#### D. Impact on the Strouhal number

We use the top-view visualizations to estimate the influence of rotation on the Strouhal number of the established Karman street. The Strouhal number is usually defined as a dimensionless frequency  $St = (DFe)/U$ , where  $Fe$  is the mean eddy-shedding frequency from one side of the cylinder. We used a geometrical method on a small number of vortices to estimate  $St = (1 - Vd/U)D/L$ , where  $Vd$  is the drifting velocity of the Karman street and  $L$  the average distance between vortices of the same sign. According to Fig. 11, the measured Strouhal number weakly decreases with the increasing Rossby number. A similar trend was also measured by Boyer *et al.*<sup>15</sup> and Boyer and Kmetz<sup>16</sup> for larger Reynolds number experiments performed on the large-scale Coriolis platform. Nevertheless, taking into account the experimental dispersion, the measured values remain very close to the two-dimensional nonrotating case<sup>23</sup> represented by a solid line in Fig. 11 for  $Re = 150$ .

#### V. DISCUSSION

Several questions arise from this research. First of all, one can ask: How will a vertical stratification affect the previous results obtained in a barotropic fluid? Could the selective destabilization of anticyclones be suppressed by the vertical stratification?

To address this question we should, here again, make the distinction between the centrifugal and the elliptical instability. A classical illustration of centrifugal instability is given by the circular Couette flow, for which the density stratification has a stabilizing effect and the vertical wavelength of the unstable mode at the onset of instability is reduced.<sup>30,31</sup> Recent numerical simulations of Kelvin–Helmholtz vortices in

a shear exhibit both a centrifugal and an elliptical branch of instability.<sup>32</sup> The rotation and stratification affect these different modes of instability unequally. In the presence of a background rotation, the centrifugal mode is rapidly stabilized when the stratification is increased, while the growth rate of the elliptical mode remains almost unchanged.<sup>32</sup> Besides, the short-wave asymptotic instability analysis of elliptical vortices in a rotating fluid had shown that the stratification does not suppress the elliptical instability for strong anticyclones. The growth rate is unchanged for horizontal plane disturbances and in some cases the stratification could even enhance the elliptical instability.<sup>33</sup> Hence, we do not expect the stratification to induce a strong stabilization of the elliptical anticyclonic structures in a rotating Karman street.

Another key question arises on the relevance of large aspect ratio  $\alpha = 4-14$  if we want to apply these results in an atmospheric or an oceanic context where  $\alpha$  is much smaller than unity. Does the three-dimensional inertial and elliptical instabilities still persist in a shallow-water context when  $h \ll D$ ? If the instabilities persist, how will the structure of the perturbation, namely, the vertical wavelength, will be affected by the small aspect ratio constraint?

To study the shallow-water case, we performed some preliminary experiments in a two-layer configuration, displacing the cylinder only in a thin upper layer. Hence, we forced the formation of a Karman street in the upper layer while the deep lower layer remained almost at rest. For practical reasons it was not possible to reach a small aspect ratio in a rotating rectangular tank only 1.5 m long. Nevertheless, we made some dye visualizations for the case  $\alpha \sim 1$  ( $h = D = 2$  cm). In Fig. 12 we clearly see that the selective destabilization of anticyclonic structures in the rotating Karman street persists when  $\alpha = 1$ ,  $Ro = 2$ , and  $Re = 150$ . The side-view visualization hardly reveals the vertical structure of the three-dimensional perturbation and no vertical wavelength could be measured.

#### VI. CONCLUSION

Our purpose in this paper was to investigate by means of laboratory experiments the three-dimensional destabilization of rotating Karman streets. We performed both dye visualizations and quantitative PIV measurements of the vorticity field. These measurements have shown that the symmetry between the cyclonic and the anticyclonic vortices in the lee of the obstacle is broken when the Rossby number, or the relative vorticity ratio  $|\omega/2\Omega_0|$ , exceeds unity. Indeed, intense anticyclonic vortices experience a transient three-dimensional destabilization while the cyclones remain always stable and coherent. This selective destabilization occurs during a few inertial periods in the initial stage of shedding when the free-shear layer, detached behind the cylinder, rolls up into an elliptical vortex. The exact nature of this secondary instability was never studied in detail. The inertial (also called centrifugal instability) is usually mentioned when initially two-dimensional anticyclonic structures are destabilized by three-dimensional perturbations in a rotating flow. However, according to our results, it is a different type of instability that controls the breaking of symmetry

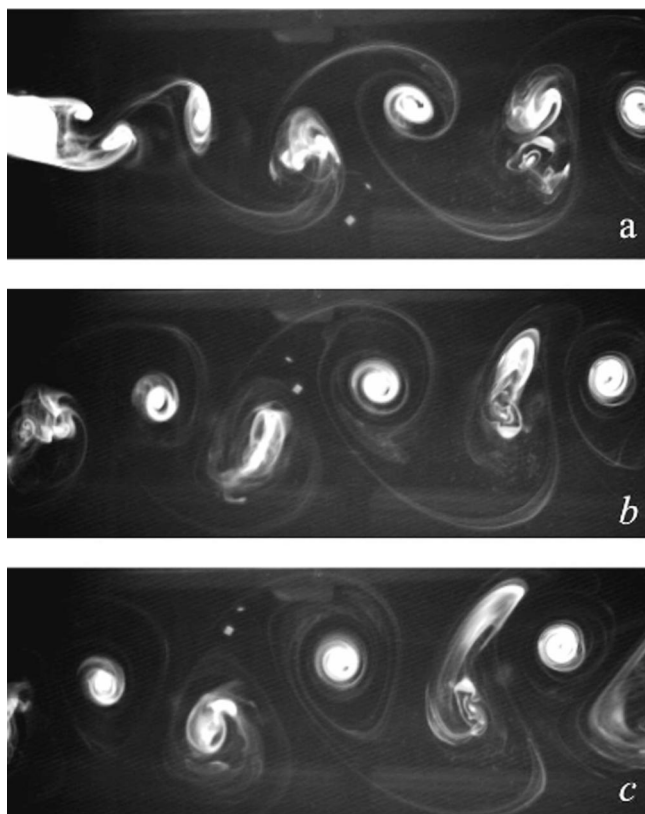


FIG. 12. Dynamical evolution of the vortex street, revealed by the fluorescent dye, in a shallow-water configuration  $\alpha=1$ ,  $Ro=2$ , and  $Re\sim 150$ . The images were taken at  $t=0$  (a),  $t=Tf$  (b), and  $t=2Tf$  (c).

in a rotating Karman street. Dye visualizations reveal that, unlike a classical centrifugal instability developing a vortex-edge perturbation, the unstable mode growing inside an anticyclonic structure is here a vortex-core perturbation. Moreover, the vertical wavelength of this perturbation increased with the Rossby number  $Ro$ . This strong influence of  $Ro$  on the wavelength selection is in reasonable agreement with the asymptotic theory of elliptical instability in rotating flows. Detailed analysis of the vorticity and the strain rate showed that the elliptical instability criterion (2) is satisfied at the early stage of vortex shedding in the region where small-scale perturbations grow rapidly. Hence, according to our results, the strong ellipticity of detached vortices behind the obstacle governs the three-dimensional instability in rotating Karman streets. The elliptical instability is, for a negative vorticity region, the dominant mechanism leading to a direct energy cascade toward small scales.

If we want to apply these results to atmospheric Karman streets we should keep in mind that in our experiment the production of vertical vorticity differs from the stratified atmosphere. In laboratory experiments the vorticity is produced by viscous boundary layers while in a stratified atmosphere the baroclinic tilting of horizontal vorticity or hydraulic jumps could dominate the production of vertical vorticity.<sup>3,6,7</sup> Nevertheless, these different mechanisms produce similar vortex wake where elliptical vortices of both signs are formed just behind the obstacle. Hence, we expect the inertial-elliptical instability we studied to be also active

for atmospheric wake. Besides, there is a significant difference in the aspect ratio  $\alpha=h/D$  between the laboratory ( $\alpha\sim 10$ ) and the atmospheric flow ( $\alpha\ll 1$ ). A first step was to perform a few experiments in a thin-layer configuration in which the aspect ratio  $\alpha$  was close to unity. In this case, according to dye visualizations, the instability was not damped by the vertical confinement, and strong three-dimensional perturbation still occurs in the negative vorticity region. Hence, if we extrapolate our results to an atmospheric flow splitting around an isolated mountain (shallow-water configuration  $\alpha\ll 1$ ), we should expect, when the Rossby number exceeds unity, small-scale divergent and vertical motions in the elliptical anticyclonic structures formed just behind the mountain. The rapid diffusion of vorticity induced by this transient instability would lead to a smaller value of anticyclonic vorticity and a stronger elongation compared to cyclonic neighbors.

## ACKNOWLEDGMENTS

The authors would like to acknowledge P. Billant and Ya. Afanasyev for valuable discussion, and R. Griffiths for a careful reading of the manuscript. This work received financial support from the CNRS program ACI-CATNAT "cyclones intenses."

- <sup>1</sup>T. P. DeFelice *et al.*, "Landsat-7 reveals more than just the surface feature in remote areas of the globe," *Bull. Am. Meteorol. Soc.* **81**, 1047 (2001).
- <sup>2</sup>D. Etling, "On atmospheric vortex street in the wake of large islands," *Meteor. Atmos. Phys.* **41**, 157 (1989).
- <sup>3</sup>R. Rotunno and P. K. Smolarkiewicz, "Further results on lee vortices in low-Froude number flow," *J. Atmos. Sci.* **48**, 2204 (1991).
- <sup>4</sup>C. Schär and R. B. Smith, "Shallow-water flow past isolated topography. Part I: Vorticity production and wake formation," *J. Atmos. Sci.* **50**, 1373 (1993).
- <sup>5</sup>C. Schär and R. B. Smith, "Shallow-water flow past isolated topography. Part II: Transition to vortex shedding," *J. Atmos. Sci.* **50**, 1401 (1993).
- <sup>6</sup>C. Schär and D. R. Durran, "Vortex formation and vortex shedding in continuously stratified flows past isolated topography," *J. Atmos. Sci.* **54**, 534 (1997).
- <sup>7</sup>V. Grubisic, R. B. Smith, and C. Schär, "The effect of bottom friction on shallow-water flow past an isolated obstacle," *J. Atmos. Sci.* **52**, 1985 (1995).
- <sup>8</sup>J. A. Johnson, "Stability of shearing motion in rotating fluid," *J. Fluid Mech.* **17**, 337 (1963).
- <sup>9</sup>S. Yanase, C. Flores, O. Metais, and J. Riley, "Rotating free-shear flows. I. Linear stability analysis," *Phys. Fluids A* **5**, 2725 (1993).
- <sup>10</sup>R. C. Kloosterziel and J. F. van Heijst, "An experimental study of unstable barotropic vortices in a rotating fluid," *J. Fluid Mech.* **223**, 1 (1991).
- <sup>11</sup>I. C. Mutabazi, C. Normand, and J. E. Wesfreid, "Gap size effects on centrifugally and rotationally driven instability," *Phys. Fluids A* **4**, 1199 (1992).
- <sup>12</sup>S. Leblanc and C. Cambon, "On the three-dimensional instabilities of plane flows subject to Coriolis force," *Phys. Fluids* **9**, 1307 (1997).
- <sup>13</sup>D. Sipp, E. Lauga, and L. Jacquin, "Vortices in rotating systems: Centrifugal, elliptic, and hyperbolic type instabilities," *Phys. Fluids* **11**, 3716 (1999).
- <sup>14</sup>E. J. Hopfinger, F. K. Browand, and Y. Gagne, "Turbulence and waves in a rotating tank," *J. Fluid Mech.* **125**, 505 (1982).
- <sup>15</sup>D. J. Boyer *et al.*, "Rotating open channel flow past right circular cylinders," *Geophys. Astrophys. Fluid Dyn.* **30**, 271 (1984).
- <sup>16</sup>D. J. Boyer and M. L. Kmetz, "Vortex shedding in rotating flows," *Geophys. Astrophys. Fluid Dyn.* **26**, 51 (1983).
- <sup>17</sup>L. Tarbouriech and D. Renouard, "Stabilisation et destabilization par la rotation d'un sillage turbulent," *C. R. Acad. Sci. III* **323**, 391 (1996).
- <sup>18</sup>Ya. D. Afanasyev and W. R. Peltier, "Three-dimensional instability of anticyclonic swirling flow in rotating fluid: Laboratory experiments and related theoretical predictions," *Phys. Fluids* **10**, 3194 (1998).

- <sup>19</sup>Ya. D. Afanasyev, "Experiments on instability of columnar vortex pairs in rotating fluid," *Geophys. Astrophys. Fluid Dyn.* **96**, 31 (2002).
- <sup>20</sup>P. Bonneton (private communication).
- <sup>21</sup>M. Lesieur, S. Yanase, and O. Métais, "Stabilizing and destabilizing effects of a solid-body rotation on quasi-two-dimensional shear layers," *Phys. Fluids A* **3**, 403 (1991).
- <sup>22</sup>P. Bartello, O. Métais, and M. Lesieur, "Coherent structures in rotating three-dimensional turbulence," *J. Fluid Mech.* **273**, 1 (1994).
- <sup>23</sup>G. F. Carnevale, M. Briscolini, R. C. Kloosterziel, and G. K. Vallis, "Three-dimensionally perturbed vortex tubes in a rotating flow," *J. Fluid Mech.* **341**, 127 (1997).
- <sup>24</sup>R. T. Pierrehumbert, "Universal short-wave instability of two dimensional eddies in an inviscid fluid," *Phys. Rev. Lett.* **57**, 2157 (1986).
- <sup>25</sup>B. J. Bayly, "Three-dimensionnal instability of elliptical flows," *Phys. Rev. Lett.* **57**, 2160 (1986).
- <sup>26</sup>C. Cambon, J. P. Benoît, L. Shao, and L. Jacquin, "Stability analysis and large eddy simulation of rotating turbulence with organized eddies," *J. Fluid Mech.* **278**, 175 (1994).
- <sup>27</sup>S. LeDizes, "Three-dimensional instability of a multipolar vortex in a rotating flow," *Phys. Fluids* **12**, 2762 (2000).
- <sup>28</sup>P. Potylitsin and W. R. Peltier, "Three-dimensional destabilization of Stuart vortices: The influence of rotation and ellipticity," *J. Fluid Mech.* **387**, 205 (1999).
- <sup>29</sup>C. Y. Wen and C. Y. Lin, "Two-dimensionnal vortex shedding of a circular cylinder," *Phys. Fluids* **13**, 557 (2001).
- <sup>30</sup>B. M. Boubnov, E. B. Gledzer, and E. J. Hopfinger, "Stratified circular Couette flow: Instability and flow regimes," *J. Fluid Mech.* **292**, 333 (1995).
- <sup>31</sup>B. L. Hua, S. Le Gentil, and P. Orlandi, "First transition in circular Couette flow with axial stratification," *Phys. Fluids* **9**, 365 (1996).
- <sup>32</sup>P. G. Potylitsin and W. R. Peltier, "Stratification effects on the stability of columnar vortices on the  $f$ -plane," *J. Fluid Mech.* **355**, 45 (1998).
- <sup>33</sup>T. Miyazaki, "Elliptical instability in a stably stratified rotating fluid," *Phys. Fluids A* **5**, 2702 (1993).